Harmonic Current Emission Estimation of Modular Multilevel Converters in MV Charging Stations

Sicheng Gong, *Student Member, IEEE*, Vladimir Ćuk, and J.F.G. Cobben

***Abstract*—This paper proposes a novel framework for modular multilevel converter (MMC) current harmonic emission estimation from medium voltage (MV) charging stations. The framework is enlightened by wave decomposition, exploiting an analytical derivation of the emission, without a time-domain model. Accordingly, voltage harmonic distribution in grids can be estimated with a frequency-domain model, using the estimated voltage-dependent current emission in the iterations. Compared to conventional time-domain simulation, such method not only enables analytical harmonic estimation integrated with a large load-flow model, but also benefits from the potential of distributed computation. A 10.5 kV grid-tied single-phase half-bridge MMC simulation case on PLECS has been implemented and investigated for comparison. Corresponding results revealed that the estimated harmonic series kept the absolute average difference to the PLECS model lower than 0.02% and a correlation ratio higher than 99.990% with the simulated ones. The effectiveness of the proposed estimation framework is successfully verified.**

***Index Terms*—Modular multilevel converter, harmonics estimation, harmonic interaction, wave decomposition.**

I. Introduction

ELECTRIC vehicle (EV) is promising to realize road transport decarbonization, and fast charging demands are being boosted correspondingly to shorten charging time and improve EV user experiences [1], [2]. With high power electronics technology developing, medium voltage (MV) fast charging scheme comes feasible and economical to meet such demands and relieve low voltage grid burdens [3]. However, caused by the switching nature of power converters, harmonic current injection from charging stations is unavoidable, impacting the distortion on MV grids instead [4], [5].

The augment of active filter employment is potential to cope with the power quality problem in MV grids [6]. Nevertheless, such strategy not only increases investment cost but also lowers grid reliability due to a raised number of semiconductors and passive components. Intended to achieve an optimal trade-off regarding the regulation capability of active filters, harmonic current injection from EV chargers needs to be quantified in advance. The selection of EV charger topology will influence its harmonic current emission directly [7]. Instead of converters with a fixed level number, MMC is extensible and considered as a suitable topology for MV fast chargers to achieve a higher withstanding voltage and operation efficiency [8], [9]. Therefore MMC-based MV fast chargers are mainly focused and grid-tied MMC current injection estimation is intended in this paper. Data-driven current harmonic estimation is widespread used in industrial practices according to prior measurement data especially considering a black-box model [10]. Electromagnetic transient (EMT) simulation is also feasible to generate current emission profiles once the white-box charger model accuracy is assumed acceptable [11], [12]. Either strategy is adopted, a complete profile needs to take a huge amount of testing scenarios into account, and the main drawback is revealed by its high time expenses for profile preparation. The profile also suffers an excessive storage burden and a short period of validity due to time-variant component parameters. Moreover, the spectrum obtained above fails to answer the impacts of those converters on grids. A time-domain model will typically not be coupled to the larger network to assess the impact, and a large network model based on load flow will commonly have an overly simplified converter model. Therefore, such profile-based strategy lacks determinacy and interpretability, proposing a request of a generalized harmonic current emission model.

A classic method for generalized current harmonic emission estimation is based on the converter impedance model. In [13], a harmonic-state-space impedance model of MMC was developed to simulate MMC harmonic behaviour, while harmonics whose orders are beyond three have been neglected. Furthermore, a complex-valued impedance model was studied to explicitly track the zero-sequence component dynamics [14]. In [15]–[17], an extended MMC model considering grid impedance and capacitor voltage ripples was proposed, intended to quantify its harmonic coupling using small signal perturbation. They have exploited the mutual impacts of grid power quality and MMC harmonic current emission based on the average model, while still limited in a single-feeder scenario. Regarding a multi-infeed AC system, a novel impedance model of MMC has been developed to quantify the converter harmonic interaction in [18].

Nevertheless, such impedance model is more suitable for harmonic stability analysis instead of harmonic emission estimation, since the impedance model accuracy can be heavily harmed by harmonics induced by modulation methods [19]. For

Manuscript received 22 December 2021; revised 10 April 2022 and 2 July 2022; accepted 10 July 2022. Date of publication 27 July 2022; date of current version 24 January 2023. This work was supported in part by the NEON (New Energy and mobility Outlook for the Netherlands) under Project 17628 and in part by NWO (the Dutch Research Council). Paper no. TPWRD-01911-2021. *(Corresponding author: Sicheng Gong.)*

The authors are with the Department of Electrical Engineering, Eindhoven University of Technology, 5612 AZ Eindhoven, Netherlands (e-mail: V.Cuk@tue.nl; J.F.G.cobben@tue.nl).

Color versions of one or more figures in this article are available at https://doi.org/10.1109/TPWRD.2022.3194111.

Digital Object Identifier 10.1109/TPWRD.2022.3194111

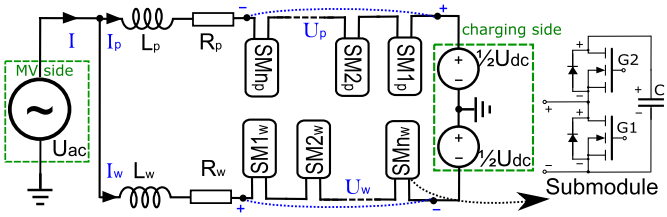

Fig. 1. Schematic of single-phase half-bridge MMC.

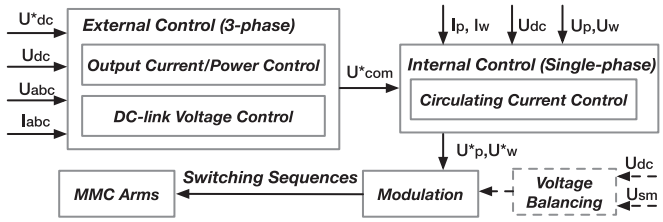

Fig. 2. Classic MMC operation framework.

a higher estimation accuracy especially in switching frequency part, Fourier decomposition over modulated submodule output voltage is unavoidable in advance of utilizing the impedance model, which would be further discussed later in this paper. The impedance model is also inconvenient to be integrated into a load-flow model for grid-level power quality investigation, in software such as DIgSILENT PowerFactory.

The motivation of this paper is to address these challenges, targeting at analytical harmonic estimation with modulation behavior considered. Therefore, this paper proposes a novel scheme to estimate MMC-based EV charger harmonic current emission based on wave decomposition, whose application in signal prediction is one of the main innovations of this paper. Wave decomposition technology has been widespread investigated and developed in recent years, while it was used for signal processing, and here it is proposed as a part of the modeling process [20], [21]. Moreover, unlike undetermined decomposed signal types in previous applications, in this paper, all decomposed signal types are predefined, including step and trigonometric functions. In this paper, such scheme aims to realize accurate and efficient estimation under a distributive or centralized framework, where modulation-induced harmonics will be pondered. This makes it possible to perform a large load-flow model integrated with analytically estimated harmonics emission. With a proper iteration algorithm, network voltage harmonic distribution estimation would be implemented as well, eventually contributing to future management suggestions for grid operators.

The remainder of this paper is organized as follows. Section II represents the general operation principle of MMC, including its modeling, controlling and modulation. Then single converter harmonic current estimation strategies are proposed and analyzed in Section III. Harmonic interaction estimation algorithm is discussed in Section IV. Simulation verification is implemented in Section V and a conclusion is provided in Section VI.

II. Modeling and Operation Principle of MMC

A. MMC Modeling

The schematic of a single-phase half-bridge MMC for MV charging is given in Fig. 1, where DC-side capacitors are simplified as a stable voltage source U_{dc} considering a potential redundant DC bus regulator. The AC-side and DC-side ground connection points are preferred to be separated to reduce common-mode noises on grids. The DC-side portal would be in series with a DC/DC converter for voltage transforming to charge EVs, while the AC-side portal is connected to MV feeders. The total conducting resistance of submodules and conduction lines are equivalent to a lumped resistor R_p or R_w in either arm, in the context of MOSFET integration and synchronous rectification. The arm inductor L_p or L_w is employed to restrict the circulating current.

Regarding grid-tied interface voltage U_{ac} and injection current I, they should follow (1). The difference between upper arm current I_p and lower arm current I_w denotes equivalent injection current to the DC link. Such equivalent current determines the DC-link injection power, which helps estimate the charging power and monitor EV charging status.

$$\begin{aligned} U_{ac} &= L_p \frac{dI_p}{dt} + R_p I_p - U_p + \frac{U_{dc}}{2} \\ U_{ac} &= L_w \frac{dI_w}{dt} + R_w I_w + U_w - \frac{U_{dc}}{2} \\ I &= I_p + I_w \end{aligned} \tag{1}$$

U_p and U_w denote relative total submodule voltage separately.

B. MMC Operation

A typical flow chart of MMC operation has been given in Fig. 2 [22]. U_{abc} and I_{abc} are measured or calculated 3-phase input voltage and current to meet power requirement. U^*_{dc} and U^*_{com} denote regulated DC-side voltage and common mode single-phase input voltage. U^*_p or U^*_w is expected equivalent total submodule voltage in either arm. U_{sm} denotes the submodule capacitor voltage.

a) Control Framework: PID controller is a classic solution for external and internal control and has been widespread adopted [23]. Such strategy would lead to predictable U^*_p and U^*_w in a normal stable operation scenario, indicating that MMC injection current in a specific steady status could be assumed countable, as soon as simplifying the whole submodule as an average model. However, due to finite submodule voltage levels, a proper modulation method is mandatory to determine switching sequences and generate asymptotic stepwise signals. Therefore, such simplification would naturally neglect harmonics caused by modulation, whose orders are commonly much higher than those intrinsically caused by controllers. That explains the main drawback of impedance modeling for converter emission estimation.

b) Modulation Technology: There exist several modulation schemes for MMC application, including phase-shift modulation (PSM), level-shift modulation, sampled average modulation, and so on [23], [24]. Voltage balancing is considered a

preliminary condition for effective modulation, which is commonly realized by sorting algorithm. Meanwhile, PSM was discussed for its natural voltage balancing property, explaining the potential omission of voltage balancing module in Fig. 2 [25]. Whereas [26] concludes that a constant bias error among submodules is highly potential under pure PSM, indicating the extra balancing module should still be kept for long-term MMC operation. Regardless of the voltage balancing module, once the modulation scheme has been determined, combined with predictable U_p^* and U_w^*, switched U_p and U_w could be forecast. In accordance with such assumption, injection harmonic current of MMC keeps theoretically calculable even based on a switching model. Switching-frequency harmonics would be counted eventually.

Focusing on harmonic estimation part, an open-loop controller is adopted to replace the PID controller for switching sequence generation, which was proved efficient as well especially with FPGA (field-programmable gate array) implementation [27]. For quasi-dynamic simulation in grid case studies, a close-loop controller can still be utilized, while its feedback period should be set long enough for the grid to move to another stable status. In summary, in this paper, U_p and U_w are assumed predictable in such open-loop or quasi-dynamic scenario, where further discussions on various controlling and modulation methods are saved.

III. Single Converter Harmonic Current Estimation

As stated in Section II, it is viable to estimate harmonic current emission from MMC-based EV chargers based on predictable switching sequences. In advance of evaluating the impacts of MMC on grid power quality, the emission of a single MMC should be estimated.

a) Step Signal Decomposition: During a steady status of MMC, controlled U_p and U_w tend to be periodic. Regarding U_p, it keeps positive in a half-bridge case while potentially becomes negative in a full-bridge case. Through decomposing U_p into a series of step or trigonometric signals as illustrated in Fig. 3, MMC connected to an ideal AC voltage source can be assumed as a linear time-invariant system, indicating the feasibility of Laplace transform for future s-domain calculation. Considering step signal decomposition, I_p in (1) becomes calculable in s-domain as illustrated in (2).

$$I_p(s) = \frac{U_{ac}(s) - \frac{U_{dc}(s)}{2} + U_p(s)}{L_p s + R_p} \tag{2}$$

where

$$U_{ac}(s) = U_{ac} \cdot \frac{\omega}{s^2 + \omega^2}$$

$$U_{dc}(s) = \frac{U_{dc}}{s}, \quad U_p(s) = \sum_{j=1}^{N} \frac{U_{\text{step}}^j}{s} e^{-T_j s} \tag{3}$$

with ω being grid angular frequency. T_j and U_{step}^j denote time delay and magnitude of a decomposed step function. Even considering control delay in practices, once such delay is predictable, T_j would keep predetermined and corresponding current harmonic emission can still be estimated.

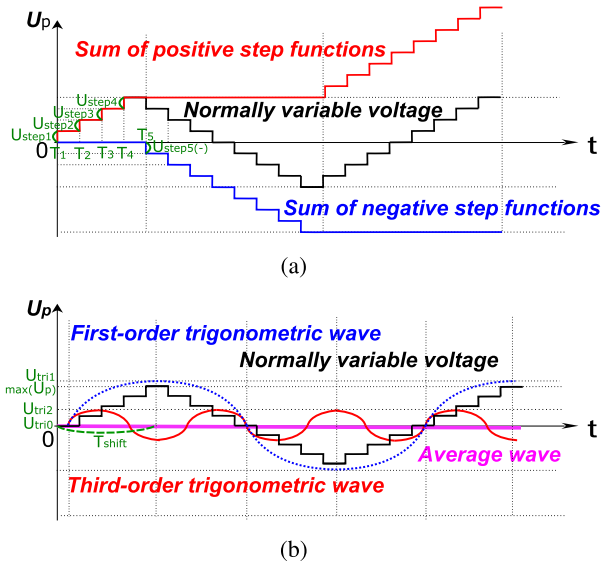

Fig. 3. Voltage wave decomposition. (a) Step decomposition. (b) Trigonometric decomposition.

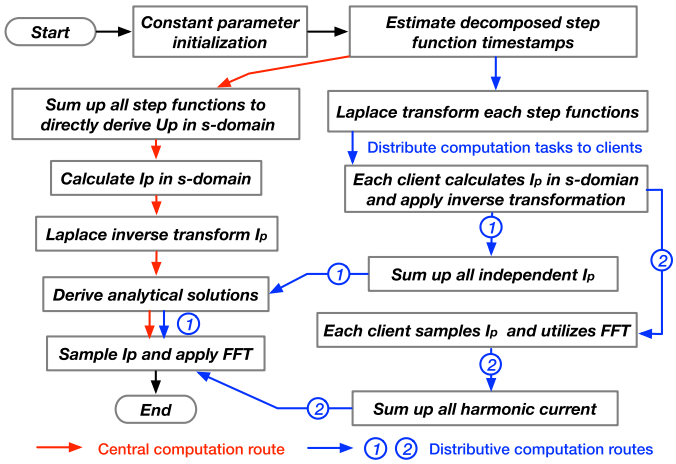

Fig. 4. Flow chart of arm current harmonic estimation.

Through symbolic calculation and inverse Laplace transform, an analytical equation representing I_p is obtained. I_w can be also derived likewise, eventually leading to calculable I. Based on estimated current waves, the spectrum can be obtained with fast Fourier transform (FFT). The analytical solution to MMC current harmonic emission is achieved eventually. The estimation accuracy is boosted by taking modulation into account, and such current spectrum is convenient for load-flow-based model integration. Under constant sampling frequency and length, such computation is advanced due to its potential to derive an analytical sensitivity coefficient regarding a specific parameter, considering the linear representability of the butterfly diagram in FFT. When those parameters vary, repetitive computation could be omitted in reference to these analytical results, which is inapplicable for conventional time-domain simulation technologies.

A flow chart based on step decomposition is given in Fig. 4 to further illustrate the estimation process and discuss its potentials for distributed computation. In a centralized framework, inverse

Algorithm 1: Accelerated Current Harmonic Estimation.

Result: $I_p^0 \cdots I_p^H$ (different-order harmonic values)
Initialize $U_{ac}, U_{dc}, R_p, L_p, U_p, t, f, f_s$;
H as maximal order, $I_p^0 \cdots I_p^H \leftarrow 0$;
$I_p^{(1)}(s) \leftarrow \frac{U_{ac}(s)-\frac{U_{dc}(s)}{2}}{L_p s+R_p}$, $I_p^{(2)}(s) \leftarrow \frac{U_{sm}}{L_p s^2+R_p s}$;
$I_p^{(1)} \leftarrow ILT(I_p^{(1)}(s))$, $I_p^{sam} \leftarrow SAM(I_p^{(1)}, t, 1/f)$;
$I_p^{(2)} \leftarrow ILT(I_p^{(2)}(s))$, $I^{sam} \leftarrow SAM(I_p^{(1)}, t, t)$;
Generate SWT_p and SWV_p based on U_p ;
for T, V ***in*** SWT_p **do**
  Set starting time $t_s \leftarrow t - T$;
  Find starting index $i_s \leftarrow t_s \cdot f_{sam}$;
  Find ending index $i_e \leftarrow (t_s + 1/f) \cdot f_{sam}$;
  $I_p^s \leftarrow V \cdot I^{sam}[i_s : i_e] + I_p^s$;
end
$I_p^0 \cdots I_p^H \leftarrow FFT(I_p^{sam})$;

Laplace transform is performed directly over the whole s-domain I_p equation, which includes all decomposed step functions. Comparatively, the s-domain I_p equation is pre-decomposed into several groups in the distributive framework, where the inverse Laplace transform is performed by each client. There exist two various decentralized working flows, distinguished by their timestamps of returning local computation results to the central processor. Since current samples own a larger data volume than a pure analytical equation, especially when a high sampling frequency is adopted, an earlier back-to-center procedure could reduce communication burden. Correspondingly, the computation capability of distributive processors is partly sacrificed. With the MMC submodule number increasing, the advantage of distributive computation can be more apparent, as the conventional time-domain simulation can be more possible to fail due to the limited computation capability of a single processor.

Even with only one processor, it is still possible to accelerate estimation by circumventing repetitive inverse Laplace transform. Algorithm 1 is listed for further illustration, where f, f_s denote fundamental and sampling frequency for FFT. $ILT(\cdot), SAM(\cdot), FFT(\cdot)$ are inverse Laplace transform, sampling and FFT functions. SWT, SWV are sequential lists containing timestamps and corresponding equivalent switched submodule quantity when U_p varies. $X[\alpha : \beta]$ denotes the fragment of a data sequence X from index α to index β. Eventually, $I_p(s)$ is divided into two parts for computation as shown in Algorithm 1, where the later one $I_p^{(2)}(s)$ can be decomposed and derived from previous computation result segments. For futher illustration, as shown in Fig. 5, response signal sequence $R(t_2)$ caused by step excitation $U(t_2)$ can be calculated directly by re-sampling $R(t_1)$.

However, Algorithm 1 is designed for open-loop controlled converter status estimation. Considering close-loop controller integration for higher system robustness, Algorithm 2 is developed, which integrates Algorithm 1 to generate a snapshot

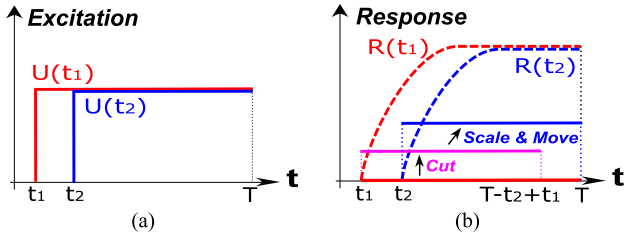

Fig. 5. Response signal sequence resampling. (a) Excitation. (b) Response.

Algorithm 2: Close-Loop Current Harmonic Estimation.

Result: $I_p^0 \cdots I_p^H$ (different-order harmonic values)
Run **Algorithm 1** to initialize $I_p^0 \cdots I_p^H$;
while *Converter is in transient status* **do**
  Extend the estimation period t;
  Run **Algorithm 1** to update $I_p^0 \cdots I_p^H$;
end
Initialize output errors;
while *Error is unacceptable* **do**
  Calculate feedbacks on certain variables;
  Update corresponding variables;
  Run **Algorithm 1** to update $I_p^0 \cdots I_p^H$;
  if *Error deviation is small enough* **then**
    Break;
  end
end

of converter status in each feedback period. Although it sacrifices the capability of transient status estimation, during quasi-dynamic estimation or simulation, the transient status itself is not mainly concerned. The close-loop feedback period in quasi-dynamic estimation is assumed long enough for equipment to move from one stable state to another one, so the effectiveness of Algorithm 2 is guaranteed.

b) Trigonometric Signal Decomposition: Under trigonometric signal decomposition as illustrated in Fig. 3(b), U_p in (3) can be updated as (4a). Through shifting U_p phase, only cosine parts in Fourier decomposition would be nonzero and harmonic phase delays are eliminated naturally if U_p owns quarter-wave symmetry. In accordance with such phase shift, $U_i(s)$ and $U_{dc}(s)$ in (3) would be changed as given by (4b).

$$U_p(s) = \sum_{j=0}^{n} \frac{U_{\text{tri}}^j \cdot s}{s^2 + (j\omega)^2} \tag{4a}$$

$$U_i(s) = U_{ac} \cdot \frac{\omega}{s^2 + \omega^2} e^{T_{\text{shift}} s},$$

$$U_{dc}(s) = \frac{U_{dc}}{s} e^{T_{\text{shift}} s} \tag{4b}$$

with U_{tri}^j being the jth order trigonometric signal magnitude. n is the highest decomposition harmonic order and and T_{shift} is U_p shifted time to ensure U_p even-symmetrical.

If U_p is quarter-wave asymmetric, its decomposed harmonic phase delays can be removed during calculation and recycled

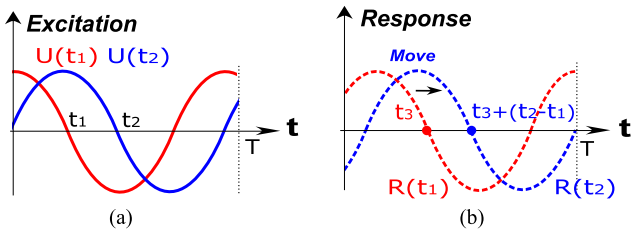

Fig. 6. Response signal sequence phase angle transfer. (a) Excitation. (b) Response.

in the final sum-up stage, which is similar to Algorithm 1. As illustrated in Fig. 6, when modulated signals vary, those voltage harmonic delays could be directly transferred and added to corresponding current spectra for acceleration Unlike repetitive resampling step-function response signals and sum them up again, those harmonic delays can be directly transferred to previously derived current spectra. This property is named "Harmonic Phase Transfer". Accordingly, the harmonic estimation based on trigonometric decomposition can be also designed distributive likewise. Moreover, such method can be further accelerated if Selective Harmonic Elimination PWM is adopted, where the modulated U_p spectrum is predetermined and corresponding FFT procedure can be saved [28].

Instead of the emphasis on equivalent impedance calculation, this estimation method mainly focuses on current harmonic emission directly, to eliminate the negative impacts of modulation on estimation accuracy. Meanwhile, except extra trigonometric decomposition over modulated U_p, the principle of such estimation is similar to that of impedance modelling method, both of which allow to compute current harmonics of each separate order through s-domain calculation. Therefore, considering the efficacy of impedance modelling method has been verified in [15], the validation of this estimation method based on trigonometric decomposition can be omitted.

c) Comparison: The main difference between these two methods, is its theoretic spectrum bandwidth. When adopting trigonometric signal decomposition, the highest decomposed sinusoidal harmonic order n determines the upper threshold of derived current spectrum bandwidth. Instead, the step decomposition technology sets no limit on final current spectrum bandwidth, which only depends on the sampling frequency of derived analytical solutions. Moreover, with accurate step function timestamps, its estimation accuracy can be boosted, while that of trigonometric decomposition is still restricted by n. Last but not least, carrier wave frequency can be a non-integer multiple of grid frequency, and they are often not connected. This makes it difficult to determine the fundamental frequency of FFT over modulated submodule voltage waves. If it happens and the fundamental frequency keeps equal to grid frequency, spectral leakage will be aggravated on switching-frequency part, eventually harming estimation accuracy.

However, step decomposition owns some comparative weakness as well. With the carrier wave frequency increasing, such method suffers a boosted computation burden, revealed by a raising number of decomposed step functions. The direct harmonic phase angle transfer is also inapplicable in step decomposition.

TABLE I
COMPARISON BETWEEN DECOMPOSITION METHODS

Index	Step signal	Trigonometric signal
Harmonic spectrum bandwidth	**Infinite**	Depend on n
Estimation accuracy	**High**	Depend on n
FFT fundamental frequency	**Flexible**	Predetermined
Computation burden	High	**Flexible**
Harmonic phase transfer capability	No	**Yes**

Table I emphasizes preferred properties by bold fonts between both methods. For a higher estimation accuracy, step decomposition is adopted, and further discussions on trigonometric decomposition are saved in this paper.

IV. HARMONIC INTERACTION ESTIMATION

The estimation method proposed in Section III can be integrated in many options for grid calculations, including power flow calculation and power quality assessment. In this section, an exemplary grid voltage harmonic calculation would be discussed. With determined harmonic current emissions from an MMC-based EV charger, corresponding voltage harmonic distribution can be calculated in reference to (5). For the observed order, relevant voltage harmonics can be calculated, where gird itself is assumed a linear time-invariant system and there exists no cross-frequency phenomenon. The fundamental-order admittance matrix can be estimated accurately by measurement data analysis, and other admittance matrices can be calculated as (5) [29], [30].

$$\mathbf{I}^h = \mathbf{Y}^h \mathbf{U}^h,\ Y_{ij}^h = \frac{1}{\mathrm{Real}(\frac{1}{Y_{ij}^1}) + h \cdot \mathrm{Imag}(\frac{1}{Y_{ij}^1})} \tag{5}$$

where $\mathbf{U}$ and $\mathbf{I}$ denote grid voltage and injection current vector. $\mathbf{Y}^h$ is the admittance matrix, whose superscript h denotes the harmonic order. Y_{ij}^h is the ith element in the jth column of $\mathbf{Y}^h$. Real$(\cdot)$ and Imag$(\cdot)$ are functions to separately extract the real and imaginary part.

Unless the converter is connected to the slack bus, according to (5), the current harmonic emission from MMC itself would distort its original point of connection (POC) voltage spectrum after its integration. Simultaneously, distorted POC voltage could change the current harmonic emission in reverse. Unfortunately, switching sequence prediction would be unavailable under such interaction due to inconstant converter POC voltage. The situation would become more complicated when multiple EV chargers are integrated. Hence, Algorithm 3 is proposed to quantify such mutual impacts by iteration, where Bus 1 is assumed as a slack bus. Instead of utilizing Newton or Quasi-Newton method to estimate voltage harmonic distribution, Gaussian-Seidel method is adopted in Algorithm 3 to ensure a stable solution [31]–[33].

Algorithm 3 can be designed distributive through allocating $I_j^{h,(i)}$ estimation tasks as shown in Fig. 7. During every iteration, each client can divide and distribute its own current harmonic estimation workload to its own salves. Under such hierarchical distributive framework, it is potential to figure outs its optimal

Algorithm 3: Voltage Harmonic Distribution Derivation.

Result: $U_2^h \cdots U_n^h$

Initialize $U_1^{1,(0)} \cdots U_n^{1,(0)}$ as original voltage, H as maximal order, $U_1^{h,(0)} \cdots U_n^{h,(0)} (h \neq 1)$ as zeros ;

$i \leftarrow 0$, ϵ is error tolerance and N is iteration constraint;

$I_1^{h,(0)} \cdots I_n^{h,(0)} \leftarrow 0$;

while $\sum_{h=0}^{H} \sum_{j=2}^{n} |U_j^{h,(i+1)} - U_j^{h,(i)}| \leq \epsilon$ *and* $i \leq N$ **do**

  Estimate $I_1^{h,(i)} \cdots I_n^{h,(i)}$ based on $U_1^{h,(i)} \cdots U_n^{h,(i)}$ as stated in Section. III ;

  Update $U_2^{h,(i+1)} \cdots U_n^{h,(i+1)}$ using $I_1^{h,(i)} \cdots I_n^{h,(i)}$ based on (5);

  $U_1^{h,(i+1)} \leftarrow U_1^{h,(i)}$, $i \leftarrow i+1$;

end

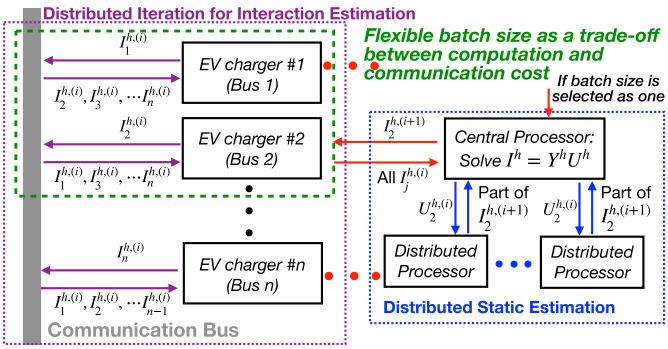

Fig. 7. Harmonic interaction estimation flow chart.

batch size in each level to achieve a trade-off between computation and communication cost.

V. Model Validation and Discussion

Intended to verify the effectiveness of proposed methods in Section III-IV, simulation based on PLECS time-domain model and estimation based on MATLAB frequency-domain computation have been implemented. Both simulation software and estimation codes were run on a computer with an Intel i7-9750H processor running at 2.60 GHz using 15.8 GB of RAM, running Windows 10 Enterprise version.

A. Single MMC Harmonic Estimation

Regarding a single-phase MMC-based EV charger in this case, it shares the same schematic as that in Fig. 1. The gate driving signals are generated as illustrated in Fig. 8, where T is the carrier period, θ and ω denote initial phase and angular frequency derived from PLL module. An open-loop controller with PSM is integrated as explained in Section II-B, whose arm current reference value is controlled by the external close-loop controller. Component and controller parameters are listed in Table II. The regulated input current in fundamental frequency is set to 20 A, and the equivalent DC-link injection current is set to 6 A. The current spectrum range is set up to 50 kHz,

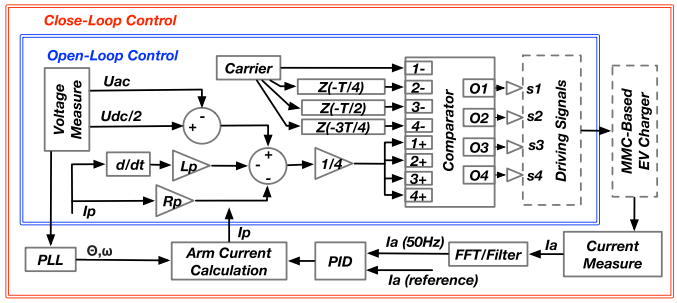

Fig. 8. Controller schematic for upper arm submodules.

TABLE II
Experimental Parameters of a Single MMC

Index	Value	Meaning
R / L	1.37Ω / 50mH	Equivalent arm resistance / inductance
U_i/U_{dc}	10.5kV / 35kV	Grid / DC side voltage magnitude
U_{sm}/N_{sm}	9kV / 8	Submodule capacitor voltage / quantity
f/f_c	50Hz / 5kHz	Grid / Modulation carrier wave frequency

TABLE III
Simulation and Estimation Results Comparison

Period(s)	Method	Time(s)	CC(%)	AAE(A)
0.02-0.04	Original	98.95	99.996	0.0019
0.02-0.04	Accelerated	1.06	99.996	0.0019
0.02-0.04	Simulation	1.25	-	-
0.98-1	Original	7085.46	99.994	0.0022
0.98-1	Accelerated	5.24	99.996	0.0025
0.98-1	Simulation	18.60	-	-

so that switching-frequency harmonics can be observed. Correspondingly, the maximum harmonic order is set to 1000 when calculating relevant admittance matrices.

At first, the MMC is set connected to a nominal AC voltage source, without any input voltage harmonics. Since the simulation starts from the zero state, it would cost a period for MMC to become stable. In this case, the stabilization period is set to 1 s referring to simulation results, indicated by close-to-zero DC part of the total current I. Accordingly, simulated current waves in $0.02\,s \sim 0.04\,s$ and $0.98s \sim 1\,s$ are sampled to observe relative harmonics from an MMC-based EV charging station during the transient and steady status. Correspondingly, harmonic estimation on the same case using step decomposition is implemented for comparative analysis.

Concerning I, corresponding estimation and simulation results are listed in Table III. The original estimation method has been illustrated by the central computation route in Fig. 4, while the accelerated one follows Algorithm 1. The estimation and simulation time expenses running on the same computer are listed. The correlation coefficient (CC) and average absolute estimation error (AAE) are indices quantifying how estimation results match simulation ones. High CCs and low AAEs in all cases prove the efficacy of proposed estimation method, including the original and accelerated ones.

a) Nominal Operation: For more details, in a period of $0.98\,s \sim 1\,s$, regarding those current harmonics derived by accelerated estimation, they have been plotted as shown in

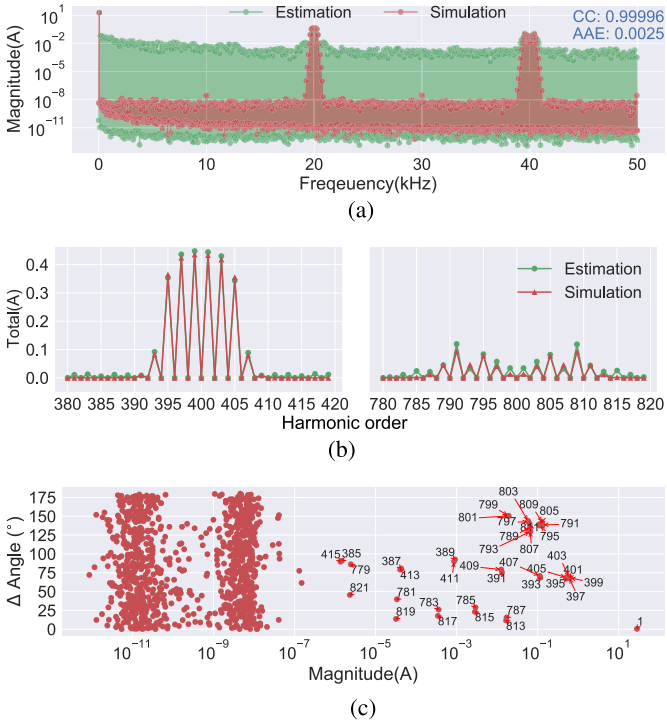

Fig. 9. MMC total current spectrum (t=0.98∼1 s). (a) Logarithmic-scale holistic spectrum. (b) Linear-scale zoomed spectrum. (c) Phase angle estimation error distribution.

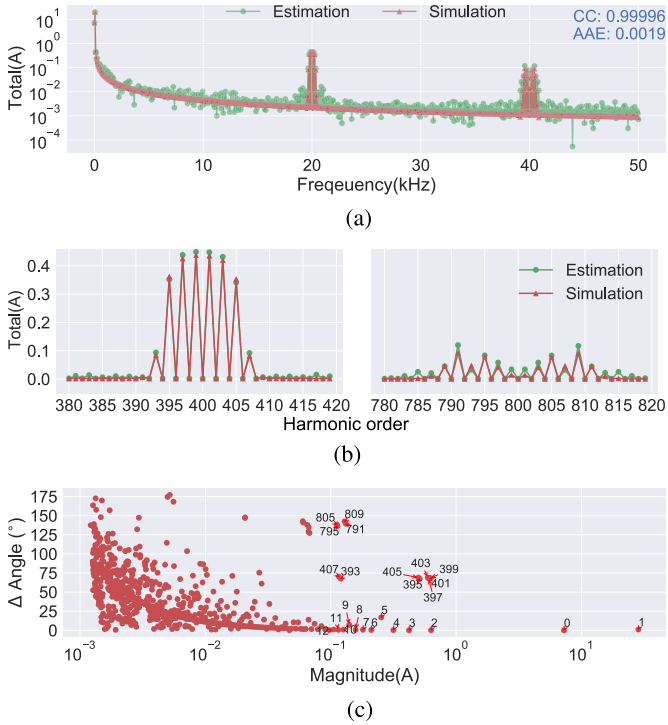

Fig. 10. MMC total current spectrum (t=0.02∼0.04 s). (a) Logarithmic-scale holistic spectrum. (b) Linear-scale zoomed spectrum. (c) Phase angle estimation error distribution.

TABLE IV
MMC LOW-FREQUENCY TOTAL CURRENT HARMONICS

Order	t=0.02s-0.04s [SIM / EST] (A)	t=0.98s-1s [SIM / EST] (A)
0	7.24 / 7.25	4.55E-9 / 9.65E-12
1	20.10 / 20.14	20.01 / 19.98
2	4.46E-1 / 4.45E-1	3.35E-9 / 2.27E-11
3	2.98E-1 / 3.11E-1	7.92E-9 / 2.91E-2
4	2.23E-1 / 2.23E-1	2.00E-9 / 7.92E-12
5	1.79E-1 / 1.76E-1	1.07E-8 / 6.64E-3
6	1.49E-1 / 1.49E-1	1.03E-9 / 7.26E-12
7	1.28E-1 / 1.24E-1	1.34E-9 / 6.50E-3
8	1.12E-1 / 1.11E-1	7.70E-10 / 3.81E-12
9	9.93E-2 / 1.01E-1	9.12E-9 / 9.16E-3
10	8.93E-2 / 8.92E-2	5.63E-10 / 2.51E-12
11	8.12E-2 / 7.46E-2	3.30E-9 / 8.09E-4

TABLE V
INDICES WITH NOMINAL VOLTAGE SOURCE

Index	t=0.02s-0.04s [SIM / EST]	t=0.98s-1s [SIM / EST]
THD	6.23% / 6.32%	5.11% / 5.23%
y(20±1kHz)	1.006A / 1.020A	1.003A / 1.016A
y(40±1kHz)	0.207A / 0.247A	0.205A / 0.244A

in Fig. 9(a). The estimated harmonics match the simulated ones well, indicated by high CCs and low AAEs. Specifically, detailed simulation (SIM) and estimation (EST) numerical value of low-frequency total current harmonics are listed for comparison in Table IV , and the estimation accuracy in low-frequency domain is verified by tolerable divergences. Concerning those considerable high-frequency harmonics induced by modulation, the spectrum is zoomed and plotted linearly as shown in Fig. 9(b), where the estimation accuracy is further confirmed by highly coincident points. Also, the simulated and estimated phase angle difference can be calculated according to (6), and corresponding scatter figures have been given in Fig. 9(c) and Fig. 10(c), where high-magnitude harmonics are annotated by their harmonic orders for illustration. In a logarithmic-scale figure, the divergence of estimated low-value harmonics is tolerable, since their relative error to fundamental part is low enough to be ignored. Regarding the total current I, the even harmonics estimation AAE is only 4.80E-11 A, while the odd one is up to 4.50E-3 A.

$$\Delta\theta = \min\{|\theta_e - \theta_s|, |\theta_e - \theta_s + 360°|, |\theta_e - \theta_s - 360°|\} \tag{6}$$

where $\Delta\theta$ denote the estimation and simulation angle difference for a specific harmonic. θ_e and θ_s are corresponding estimated and simulated angles.

Due to the uncertain sampling frequency in simulation software PLECS, the spectrum leakage is inevitable and contributes to the spectrum difference. More indices are imported to deal with such uncertainty. Corresponding total harmonic distortion (THD) derived by estimation and simulation are listed in Table V, and the difference is considered acceptable. There lacks an official standard to assess superharmonic whose frequency is beyond 9 kHz, while IEC 61000-4-7 is under consideration for extension to the 9-150 kHz range. Therefore, an extended assessment index referring to IEC 61000-4-7 is adopted to assess superharmonic beams as illustrated in (7), where a and b denote the center frequency and bandwidth of each frequency segment, and f is the fundamental frequency [34]. $y(j\text{Hz})$ is the value

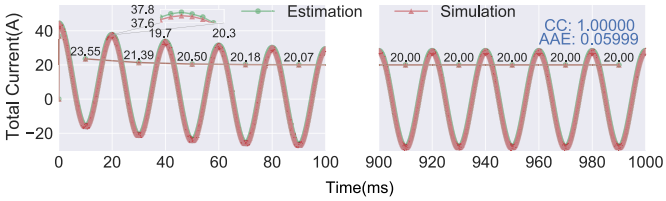

Fig. 11. Time-domain simulated and estimated current waves.

of jHz harmonic derived by FFT. Referring to IEC 61000-4-30, the frequency segment bandwidth is set 2 kHz, and the center frequency is selected as 20 kHz and 40 kHz in accordance with two peaks in Fig. 9(a) [35]. As listed in Table V, the difference of this superharmonic assessment index derived by estimation and simulation is assumed tolerable as well.

$$y\left(a \pm \frac{b}{2}\text{Hz}\right) = \sqrt{\sum_{j=a-\frac{b}{2},f}^{a+\frac{b}{2}} y^2(j\text{Hz}) - \frac{1}{2}y^2\left(a+\frac{b}{2}\text{Hz}\right) - \frac{1}{2}y^2\left(a-\frac{b}{2}\text{Hz}\right)} \tag{7}$$

When it comes to $0.02s \sim 0.04\,s$ under accelerated estimation, relative low-frequency results are also listed in Table IV. The total divergence is low as well, and odd harmonics remain a higher variance. Moreover, coincident points in the zoomed spectrum as shown in Fig. 10, together with a high CC and low AAE referring to the whole spectrum, prove the validity of the proposed estimation method. The signals restored in the time domain and respective single-cycle RMS values are plotted in Fig. 11. Through taking the simulated single-cycle RMS value as a converter stable status criterion and setting its threshold 20 ± 0.1 A, as the RMS value reaches 21.39 A, the period of $0.02\,s \sim 0.04\,s$ is judged as a transient period. Moreover, by zooming out the fragment of $19.7\,ms \sim 20.3\,ms$, the peak value is over 37.6 A, which is higher than nominal value 28.28 A, eventually further supporting such judgement. Therefore, the converter is confirmed in a transient status in $0.02\,s \sim 0.04\,s$, and the capability of transient status estimation in the open-loop scenario has been verified accordingly.

THDs and superharmonic assessment indices separately derived by estimation and simulation are listed in Table V. The THD difference is still mainly caused by low-frequency parts, and all estimated indices keep close to simulated ones. Although the high-frequency current harmonics is relatively low in this case, the grid operator will still ask for rechecking these appliances before integration, and estimation is one way to check.

b) Operation Under AC-Side Harmonics and DC-Side Ripples: Considering imperfect grid voltage and limited DC link regulation capacity, the charger POC voltage is assumed distorted with harmonics on both AC and DC links in this part. On the AC side, harmonics whose orders are equal to 3 and 5 are set 5% and 6%. Both harmonics phase angles are set zero and total harmonic distortion is equal to 7.81%, which is on the edge of violating grid code [36]. Besides, according to [37], the DC link ripple can be assumed 100 Hz sinusoidal wave in EV charging scenarios, and its magnitude can be set to 1%. Algorithm 1 is employed for computation acceleration.

TABLE VI
DISTORTED LOW-FREQUENCY TOTAL CURRENT HARMONICS

Order	t=0.02s-0.04s [SIM / EST] (A)	t=0.98s-1s [SIM / EST] (A)
0	9.41 / 9.39	1.25E-8 / 4.09E-11
1	20.13 / 20.18	20.01 / 20.01
2	5.80E-1 / 5.78E-1	2.75E-9 / 1.51E-12
3	3.87E-1 / 4.01E-1	1.61E-6 / 1.28E-2
4	2.90E-1 / 2.89E-1	9.97E-10 / 1.74E-11
5	2.34E-1 / 2.32E-1	3.22E-6 / 6.48E-3
6	1.93E-1 / 1.93E-1	1.24E-9 / 9.48E-12
7	1.66E-1 / 1.68E-1	1.89E-8 / 3.76E-3
8	1.45E-1 / 1.45E-1	6.55E-10 / 9.17E-12
9	1.29E-1 / 1.28E-1	1.97E-8 / 8.23E-3
10	1.16E-1 / 1.16E-1	8.56E-10 / 7.34E-12
11	1.06E-1 / 1.06E-1	2.93E-8 / 6.43E-3

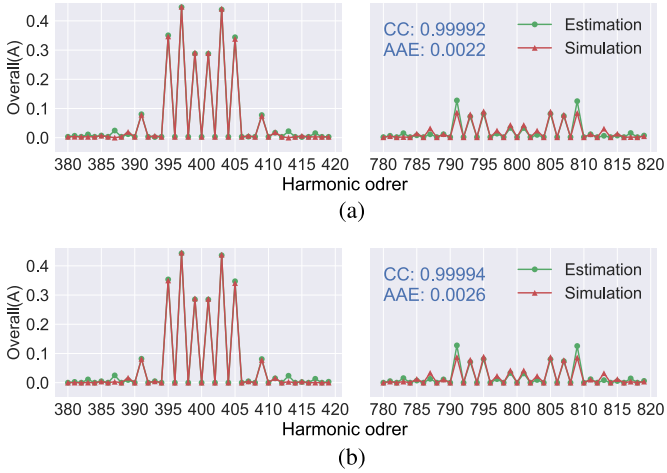

Fig. 12. Distorted simulation and estimation current. (a) $t = 0.02\,s \sim 0.04\,s$. (b) $t = 0.98\,s \sim 1.00\,s$.

TABLE VII
INDICES WITH DISTORTED VOLTAGE SOURCE

Index	t=0.02s-0.04s [SIM / EST]	t=0.98s-1s [SIM / EST]
THD	6.53% / 6.56%	4.63% / 4.65%
y(20±1kHz)	0.901A / 0.902A	0.899A / 0.899A
y(40±1kHz)	0.226A / 0.244A	0.224A / 0.242A

Distinguished by DC part value of I, $0.02s \sim 0.04\,s$ and $0.98s \sim 1s$ are considered transient and steady periods during converter operation. Corresponding simulated and estimated numerical values of low-order harmonics have been listed in Table VI. The estimation deviations remain tolerable. Regarding the stable-state simulation results, odd harmonics are augmented by relative input voltage harmonics, leading to raised values compared to those in Table IV. Meanwhile, the estimation results exhibit no such phenomenon. As shown in Fig. 12, in both steady and transient states, the estimation accuracy remains acceptable according to low AAEs and high CCs. Estimated and simulated THDs and superharmonic assessment indices are given in Table VII, and those differences are assumed tolerable referring to nominal input current.

TABLE VIII
CURRENT SPECTRUM COMPARISON (59.98-60 S)

Control Type	50-Hz part [SIM / EST]	AAE (A)	CC (%)
Open-loop	23.05A / 23.11A	0.0022	99.996
Close-loop	20.00A / 19.99A	0.0025	99.995

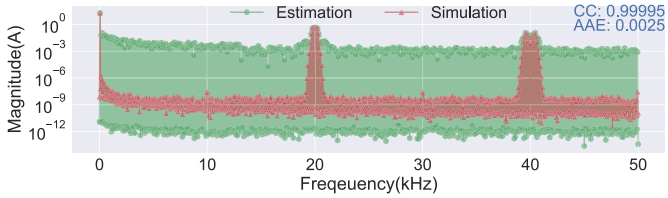

Fig. 13. Total current spectrum (Close-loop, 59.98-60 s).

TABLE IX
CLOSE-LOOP ESTIMATION AND SIMULATION TIME

Computation round	Estimation time	Simulation time
1	6.68s	22.78s
2-60 (Average)	0.60s	17.68s

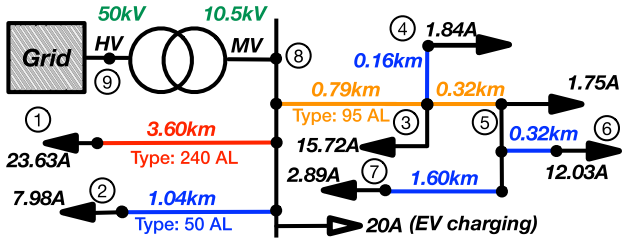

Fig. 14. MV grid schematic.

c) Operation With Close-Loop Controllers: Compared to open-loop scenarios, the close-loop controller is expected for higher robustness to model uncertainties, for instance measurement data error and component parameter variation. Both simulation and estimation models have been established for close-loop controlling as shown in Fig. 8. The close-loop feedback will be applied based on a fixed period, which is long enough for the converter to switch between stable states. In this case, the PID feedback period is set to 1 s, and the total running time is set to 1 min. Regarding the PLL integration, which plays a role of phase detector, its feedback period is set to 1 s to avoid overstretching the estimator. With a strong grid connection, its detected phase error can be assumed negligible during estimation.

During testing, it is assumed that the measured AC voltage level has dropped 1% from the nominal input voltage, while the open-loop controller failed to detect such change. Modulated switching sequences will keep, and the fundamental-frequency part of input total current will become excessive. Instead, by integrating a close-loop controller with the proportional and integral coefficient being 1.2 and 2, such fundamental-frequency part has been corrected as shown in Table VIII. This close-loop controller advances in its immunity to immeasurable AC voltage level distortions. Combining Table VIII and Fig. 13, the effectiveness of close-loop estimation scheme has been verified. Intended to quantify the estimation deviation, relative AAE is utilized, which defined by the ratio of AAE to fundamental-frequency value. The maximal relative AAE is found regarding the open-loop converter current spectrum, which keeps lower than 0.02%.

d) Parametric Computation: With charging demand varying or component degrading, the converter operation status will change accordingly. In conventional time-domain simulation, repetitive simulation is inevitable when modelling parameters vary, eventually leading to huge time expenses in total. Instead, by utilizing previously derived analytical solutions and substituting various values to a certain parameter, it is potential to omit repetitive computation and accelerate subsequent estimations.

In this part, we inherited the testing case from the close-loop scenario, and assumed the input voltage as a variable. After the first-round parametric calculation, the analytical solution can be recycled. Through allocating a different value to parameter U_{ac}, the corresponding estimation result would be derived. Regarding this testing case, computation time expenses for estimation and simulation are listed in Table IX. Based on first-round analytical results, estimation in left rounds can be implemented quickly by reusing analytical solutions. Comparatively, the time-domain simulation technology has no such property. Therefore, the potential of omitting repetitive computation has been confirmed in the proposed estimation scheme.

e) Summary: In summary, all estimation methods based on step function decomposition in Section III have been verified. Although the theoretical divergence should be infinitesimal, there exist several factors contributing to the experimental divergence: The step size when determining timestamps of step functions is set to 1E-7 s, leading to inevitable estimation timestamp errors; The simulation software step size is dynamic, whose maximum value is set 1E-6 s, contributing to inevitable sampling errors; The simulation relative tolerance is set 1E-3, indicating intrinsic simulation errors. The accelerated method benefits a lighter computation burden than the original one. Furthermore, the accelerated estimation speed even exceeds than the simulation one on PLECS. With more processors, the advantage of distributive computation feasibility would become apparent, and the estimation speed advantage would be deeply exaggerated.

B. Harmonic Estimation in Grids

Intended to explore the validity of harmonic interaction estimation in Section IV, an existing Dutch MV grid with the voltage level of 10.5 kV is selected as shown in Fig. 14. Node 9 is assumed as a slack bus to power the whole grid. All existing loads share the same power factor of 0.98, and accordingly they were converted into constant passive components for modeling simplification. An MMC-based EV charging station is connected to Node 8 with nominal input current being 20 A. More network parameters are given in Appendix.

a) Operation Without Network Parameter Deviations: As illustrated in Algorithm 3, an iteration method is adopted for iterative harmonic estimation. Intended to ensure the estimation ans simulation accuracy in the grid case, both the step function timestamp resolution and the simulation maximal step size are

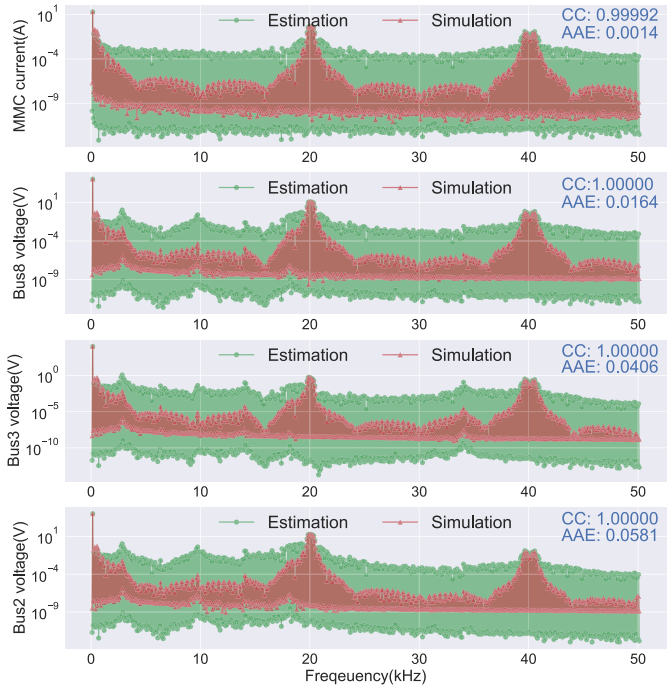

Fig. 15. Simulated and estimated network status.

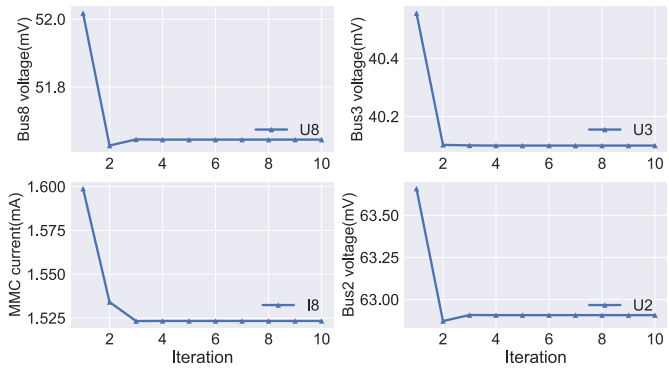

Fig. 16. AAE variation during iterations.

set to 1E-7 s accordingly. Referring to simulation results, all node voltage levels become stable after 1 s. Therefore, during each iteration, the MMC current estimation period is set to 1 s, which is long enough for converter to become stable. After 5 iterations, relative estimation results are recorded and compared to simulated ones as illustrated in Fig. 15. The estimation AAE converges indicated by its oscillation restricted in a small range as shown in Fig. 16. Such oscillation is assumed tolerable, as its absolute value is relatively low compared to the nominal value. Eventually, the efficacy of iterative estimation method proposed in Section IV has been verified.

b) Operation With Network Parameter Deviations: Intended to exploit the impacts of network parameter deviation on harmonic interaction, the grid input impedance, which is equal to the impedance between Bus 8 and Bus 9, is selected as a variate. In this case, compared to the original grid, the grid input impedance varies from 100% to 200%. According to testing results in Table X, with feeder input impedance increasing, the fundamental part of converter input voltage can be influenced.

TABLE X
BUS-8 VOLTAGE WITH GRID IMPEDANCE VARYING

Index	Value		
Feeder impedance	100%	150%	200%
50Hz-part [SIM]	10501.26V	10501.89V	10502.51V
50Hz-part [EST]	10501.24V	10501.86V	10502.50V

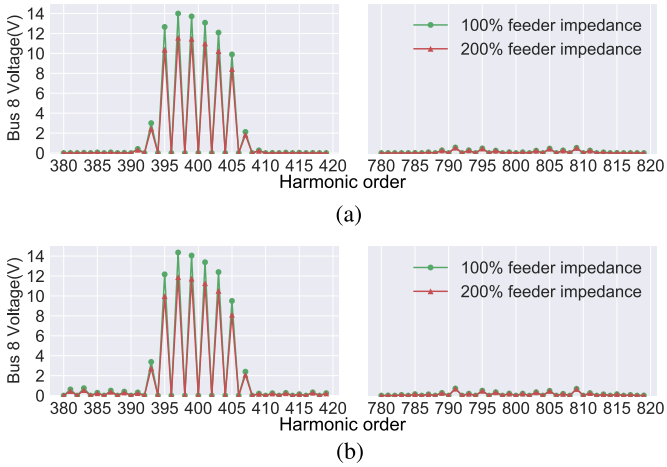

Fig. 17. Part of Bus 8 voltage spectrum (0.98-1 s). (a) Simulation results. (b) Estimation results.

Moreover, Bus 8 voltage spectrum has changed accordingly as shown in Fig. 17. Those phenomena have confirmed the impacts of network parameters on simulation and estimation results. Meanwhile, based on same network parameters, the estimation results are still close to the simulated ones, emphasizing the estimation accuracy.

VI. CONCLUSION

This article has presented a novel scheme for harmonic current emission estimation from MMC-based EV charging stations. Enlightened by wave decomposition, such scheme transform the MMC submodule as a linear time-invariant subsystem. Through taking modulation into consideration, it not only derives analytical solutions with a higher theoretical accuracy than conventional impedance modeling method, but also allows analytical solutions to current harmonic emissions. Such analytical solution is convenient for load-flow model integration, eventually helping answer the impacts of chargers on grid power quality. Regarding the verification part, during single MMC harmonic estimation, the accelerated estimation time expense is even lower than the simulation one. With the potential of distributive computation, such estimation scheme can be further accelerated. Finally, the highly matched estimation results compared to simulated ones illustrate the efficacy of proposed methods, whose minimal CC and maximal relative AAE in all cases are high than 99.990% and lower than 0.02%.

In the future, transient close-loop-controlled MMC current harmonic emission would be exploited. Moreover, harmonic current interaction in a larger network should be further investigated as well, to achieve a higher estimation accuracy in the premise of iteration convergence.

APPENDIX
MV DUTCH GRID CASE PARAMETER

The Π-model is adopted for power cable modeling, with ground capacitance being 0.2929 μC/km. Cable and transformer impedance are listed as below.

TABLE XI
POWER CABLE AND TRANSFORMER PARAMETERS

Object	Resistance	Reactance (50Hz)
240 AL Cable	126mΩ/km	116mΩ/km
95 AL Cable	320mΩ/km	188mΩkm
50 AL Cable	641mΩ/km	204mΩ/km
36MVA Transformer (50kV/10.5kV)	0.0022p.u.	0.065p.u.

ACKNOWLEDGMENT

The authors would like to acknowledge Prof. C.G.E. (Korneel) Wijnands and Dr. Dongsheng Yang at TU/e for software support and nice comments.

REFERENCES

[1] I. E. Agency, "Global EV outlook 2022: Securing supplies for an electric future," *IEA*, 2022. [Online]. Available: https://www.iea.org/reports/global-ev-outlook-2022
[2] A. Hoekstra and N. Refa, "Characteristics of dutch EV drivers," in *Proc. 30th Int. Electric Veh. Symp. Exhib.*, 2017, pp. 2–6.
[3] Y. Tahir et al., "A state-of-the-art review on topologies and control techniques of solid-state transformers for electric vehicle extreme fast charging," *IET Power Electron.*, vol. 14, pp. 560–1576, 2021.
[4] Y. Sun, E. De Jong, V. Cuk, and J. Cobben, "Harmonic resonance risk of massive ultra fast charging station grid integration," in *Proc. 18th Int. Conf. Harmon. Qual. Power*, 2018, pp. 1–6.
[5] Y. Zhang, D. Yu, G. Zhang, H. Wang, and J. Zhuang, "Harmonic analysis of EV charging station based on measured data," in *Proc. IEEE/IAS Ind. Commercial Power Syst. Asia*, 2020, pp. 475–480.
[6] L. Wang, C.-S. Lam, and M.-C. Wong, "Hybrid structure of static VAR compensator and hybrid active power filter (SVC//HAPF) for medium-voltage heavy loads compensation," *IEEE Trans. Ind. Electron.*, vol. 65, no. 6, pp. 4432–4442, Jun. 2018.
[7] H. Tu, H. Feng, S Srdic, and S. Lukic, "Extreme fast charging of electric vehicles: Atechnology overview," *IEEE Trans. Transport. Electrific.*, vol. 5, no. 4, pp. 861–878, Dec. 2019.
[8] L. Camurca, X. Gao, L. F. Costa, and M. Liserre, "Design of a medium voltage DC fast charging station with grid voltage regulation and central modular multilevel converter," in *Proc. IEEE Energy Convers. Congr. Expo.*, 2018, pp. 2798–2804.
[9] Y. P. Marca, M. G. Roes, J. L. Duarte, and K. G. Wijnands, "Isolated MMC-based AC/AC stage for ultrafast chargers," in *Proc. IEEE 30th Int. Symp. Ind. Electron.-Kyoto*, 2021, pp. 1–8.
[10] T. Slangen, T. van Wijk, V. Ćuk, and J. Cobben, "The harmonic and supraharmonic emission of battery electric vehicles in The Netherlands," in *Proc. Int. Conf. Smart Energy Syst. Technol.*, 2020, pp. 1–6.
[11] D. Shu, H. Yang, and G. He, "A harmonic phasor domain cosimulation method and new insight for harmonic analysis of large-scale VSC-MMC based AC/DC grids," *IEEE Trans. Power Electron.*, vol. 36, no. 4, pp. 3909–3924, Apr. 2021.
[12] J. Peralta, H. Saad, S. Dennetière, J. Mahseredjian, and S. Nguefeu, "Detailed and averaged models for a 401-level MMC-HVDC system," *IEEE Trans. Power Del.*, vol. 27, no. 3, pp. 1501–1508, Jul. 2012.
[13] J. Lyu, X. Zhang, X. Cai, and M. Molinas, "Harmonic state-space based small-signal impedance modeling of a modular multilevel converter with consideration of internal harmonic dynamics," *IEEE Trans. Power Electron.*, vol. 34, no. 3, pp. 2134–2148, Mar. 2019.
[14] H. Wu and X. Wang, "Dynamic impact of zero-sequence circulating current on modular multilevel converters: Complex-valued AC impedance modeling and analysis," *IEEE Trans. Emerg. Sel. Topics Power Electron.*, vol. 8, no. 2, pp. 1947–1963, Jun. 2020.
[15] Z. Xu et al., "A complete HSS-based impedance model of MMC considering grid impedance coupling," *IEEE Trans. Power Electron.*, vol. 35, no. 12, pp. 12929–12948, Dec. 2020.
[16] K. Ji, G. Tang, H. Pang, and J. Yang, "Impedance modeling and analysis of MMC-HVDC for offshore wind farm integration," *IEEE Trans. Power Del.*, vol. 35, no. 3, pp. 1488–1501, Jun. 2020.
[17] Z. Li et al., "Accurate impedance modeling and control strategy for improving the stability of DC system in multiterminal MMC-based DC grid," *IEEE Trans. Power Electron.*, vol. 35, no. 10, pp. 10026–10049, Oct. 2020.
[18] Y. Chen, L. Xu, A. Egea-Àlvarez, B. Marshall, M. Rahman, and O. D. Adeuyi, "MMC impedance modelling and interaction of converters in close proximity," *IEEE Trans. Emerg. Sel. Topics Power Electron*., vol. 9, no. 6, pp. 7223–7236, Dec. 2021.
[19] K. Shen et al., "Elimination of harmonics in a modular multilevel converter using particle swarm optimization-based staircase modulation strategy," *IEEE Trans. Ind. Electron.*, vol. 61, no. 10, pp. 5311–5322, Oct. 2014.
[20] A. Cicone, J. Liu, and H. Zhou, "Adaptive local iterative filtering for signal decomposition and instantaneous frequency analysis," *Appl. Comput. Harmon. Anal.*, vol. 41, no. 2, pp. 384–411, 2016.
[21] A. Cicone, M. Huska, S.-H. Kang, and S. Morigi, "JOT: A variational signal decomposition into jump, oscillation and trend," *IEEE Trans. Signal Process.*, vol. 70, pp. 772–784, 2022.
[22] R. Darus, "Modulation and control of modular multilevel converters," Ph.D. dissertation, Univ. New South Wales, Sydney NSW, Australia, 2015.
[23] S. Debnath, J. Qin, B. Bahrani, M. Saeedifard, and P. Barbosa, "Operation, control, and applications of the modular multilevel converter: A review," *IEEE Trans. Power Electron.*, vol. 30, no. 1, pp. 37–53, Jan. 2015.
[24] S. Du, A. Dekka, B. Wu, and N. Zargari, *Modular Multilevel Converters: Analysis, Control, and Applications*. Hoboken, NJ, USA: Wiley, 2017.
[25] L. Mathe, P. D. Burlacu, and R. Teodorescu, "Control of a modular multilevel converter with reduced internal data exchange," *IEEE Trans. Ind. Informat.*, vol. 13, no. 1, pp. 248–257, Feb. 2017.
[26] W. van der Merwe, P. Hokayem, and L. Stepanova, "Analysis of the N-cell single phase MMC natural balancing mechanism," *IEEE Trans. Emerg. Sel. Topics Power Electron.*, vol. 2, no. 4, pp. 1149–1158, Dec. 2014.
[27] R. O. Fatunmbi, O. O. Okoye, O. A. Lasabi, and I. E. Davidson, "FPGA implementation of open-loop controller for five-level three phase modular multilevel converter," in *Proc. IEEE AFRICON*, 2017, pp. 1345–1350.
[28] M. S. Dahidah, G. Konstantinou, and V. G. Agelidis, "A review of multilevel selective harmonic elimination PWM: Formulations, solving algorithms, implementation and applications," *IEEE Trans. Power Electron.*, vol. 30, no. 8, pp. 4091–4106, Aug. 2015.
[29] J. Zhang, P. Wang, and N. Zhang, "Distribution network admittance matrix estimation with linear regression," *IEEE Trans. Power Syst.*, vol. 36, no. 5, pp. 4896–4899, Sep. 2021.
[30] R. K. Gupta, F. Sossan, J.-Y. Le Boudec, and M. Paolone, "Compound admittance matrix estimation of three-phase untransposed power distribution grids using synchrophasor measurements," *IEEE Trans. Instrum. Meas.v*, vol. 70, pp. 1–13, 2021.
[31] C. D. Collins, "Facts device modelling in the harmonic domain," Ph.D. dissertation, Univ. Canterbury, 2006. [Online]. Available: http://hdl.handle.net/10092/1103
[32] K. L. Lian and P. W. Lehn, "Steady-state solution of a voltage-source converter with full closed-loop control," *IEEE Trans. Power Del.*, vol. 21, no. 4, pp. 2071–2081, Oct. 2006.
[33] M. Esparza, J. Segundo-Ramirez, J. B. Kwon, X. Wang, and F. Blaabjerg, "Modeling of VSC-based power systems in the extended harmonic domain," *IEEE Trans. Power Electron.*, vol. 32, no. 8, pp. 5907–5916, Aug. 2017.
[34] "*Electromagnetic compatibility (EMC) -part 4-7: testing and measurement techniques*," International Electrotechnical Commission, Standard IEC 61000-4-7:2009, 2009.
[35] "*Electromagnetic compatibility (EMC) -part 4-30: testing and measurement techniques*," International Electrotechnical Commission, Standard IEC 61000-4-30:2015, 2015.
[36] J. Cobben, D. Geldtmeijer, A. Almering, and J. van Waes, "Evaluation and updating of harmonic voltage limits," in *Proc. IEEE Eindhoven PowerTech*, 2015, pp. 1–5.
[37] D. B. W. Abeywardana, P. Acuna, B. Hredzak, R. P. Aguilera, and V. G. Agelidis, "Single-phase boost inverter-based electric vehicle charger with integrated vehicle to grid reactive power compensation," *IEEE Trans. Power Electron.*, vol. 33, no. 4, pp. 3462–3471, Apr. 2018.

Sicheng Gong (Student Member, IEEE) received the B.Eng. degree in electrical engineering from Shanghai Jiao Tong University, Shanghai, China, and the M.Sc. degree in electrical engineering from the Technical University of Denmark, Kongens Lyngby, Denmark. He is currently working toward the Ph.D. degree from the Eindhoven University of Technology, Eindhoven, The Netherlands, focusing on power quality management considering MV fast-charging. During this period, his works were related to network optimization, topology design, and cyber-physical security. His research interests inlcude converter and power unit modeling, controller designing, and charger deployment planning.

Vladimir Ćuk received the Dipl.Ing. (M.Sc.) degree in electrical engineering from the School of Electrical Engineering, University of Belgrade, Belgrade, Serbia, in 2005, and the Ph.D. degree from the Electrical Energy Systems Group, Eindhoven University of Technology, Eindhoven, The Netherlands, in 2013. From 2006 to 2009, he was with the Department of Electrical Measurements, Electrical Engineering Institute Nikola Tesla, Belgrade, Serbia. He is currently an Assistant Professor with the Eindhoven University of Technology. His research interests include electrical power quality and the long term impacts of network changes, and energy use and generation on the supply quality.

J.F.G. (Sjef) Cobben received the master's degree in electrical engineering from the Eindhoven University of Technology (TU/e), Eindhoeven, The Netherlands, (with the distinction cum laude), in 2002. He is currently a Professor of power quality with the Research Group Electrical Energy Systems, TU/E Department of Electrical Engineering. From 2003 to 2007, he performed part-time Ph.D. research with the same university, resulting in his 2007 thesis Power Quality, Implications at the Point of Connection. In 2009, he founded the company CO-Education, providing knowledge services and education in the field of electrical engineering, in particular regarding power quality, smart grids, and sustainability of the electricity supply. In 2011, he was appointed part-Time Professor of power quality with the TU&e Department of Electric Engineering, Research Group Electrical Energy systems. His areas of expertise are LV- and MV-network safety, power quality and safety of installations connected to the networks. His TU-e research theme of powerquality concerns the quality of voltage, current, and their mutual interaction. This is of relevance to smart grid technologies, integration of renewable energy sources, and compatibility of devices, installations and networks.